

# Prototyping and characterisation of 316L stainless steel parts and lattice structures printed via metal fused filament fabrication

*Ludovico Martignoni and Andrea Vegro*

School of Industrial and Information Engineering, Politecnico di Milano, Milan, Italy

*Sara Candidori*

Department of Mechanical Engineering, Politecnico di Milano, Milan, Italy

*Mohammad Qasim Shaikh and Sundar V. Atre*

Department of Mechanical Engineering, University of Louisville, Louisville, Kentucky, USA, and

*Serena Graziosi and Riccardo Casati*

Department of Mechanical Engineering, Politecnico di Milano, Milan, Italy

## Abstract

**Purpose** – This study aims to deepen the knowledge concerning the metal fused filament fabrication technology through an analysis of the printing parameters of a commercial 316L stainless steel filament and their influence on the porosity and mechanical properties of the printed parts. It also investigates the feasibility of manufacturing complex geometries, including strut-and-node and triply periodic minimal surface lattices.

**Design/methodology/approach** – A three-step experimental campaign was carried out. Firstly, the printing parameters were evaluated by analysing the green parts: porosity and density measurements were used to define the best printing profile. Then, the microstructure and porosity of the sintered parts were investigated using light optical and scanning electron microscopy, while their mechanical properties were obtained through tensile tests. Finally, manufacturability limits were explored with reference samples and cellular structures having different topologies.

**Findings** – The choice of printing parameters drastically influences the porosity of green parts. A printing profile which enables reaching a relative density above 99% has been identified. However, voids characterise the sintered components in parallel planes at the interfaces between layers, which inevitably affect their mechanical properties. Lattice structures and complex geometries can be effectively printed, debinded, and sintered if properly dimensioned to fulfil printing constraints.

**Originality/value** – This study provides an extensive analysis of the printing parameters for the 316L filament used and an in-depth investigation of the potential of the metal fused filament fabrication technology in printing lightweight structures.

**Keywords** Metal fused filament fabrication, Design for additive manufacturing, 316L stainless steel, Lattice structures, Triply periodic minimal surface, Printing parameters

**Paper type** Research paper

## 1. Introduction

Fused filament fabrication (FFF) is the most common and widely used additive manufacturing (AM) technology (Cuan-Urquizo *et al.*, 2019). Nowadays, the presence on the market of 3D printers able to reach high temperatures allows to extend its use to different materials, including composites, ceramics, and metals (Gonzalez-Gutierrez *et al.*, 2018; Suwanpreecha and Manonukul, 2022; Wagner *et al.*, 2022). Thus, the wide variety of available materials can help FFF to compete with well-established manufacturing processes. New materials can make the production of functional prototypes and small components more affordable than with other AM technologies (Liu *et al.*,

2020; Suwanpreecha and Manonukul, 2022). Recently, we have been assisting a growing interest in the 3D printing of

---

© Ludovico Martignoni, Andrea Vegro, Sara Candidori, Mohammad Qasim Shaikh, Sundar V. Atre, Serena Graziosi and Riccardo Casati. Published by Emerald Publishing Limited. This article is published under the Creative Commons Attribution (CC BY 4.0) licence. Anyone may reproduce, distribute, translate and create derivative works of this article (for both commercial & non-commercial purposes), subject to full attribution to the original publication and authors. The full terms of this licence may be seen at <http://creativecommons.org/licenses/by/4.0/legalcode>

The authors acknowledge Antonio Sabatti, CEO of Metrocast Italiana S.p.a ([www.metrocast.it](http://www.metrocast.it)), for his technical and operative support in the debinding and sintering processes of the samples and lattices.

The Italian Ministry of Education, University and Research is acknowledged for the support provided through the Project “Department of Excellence LIS4.0 – Lightweight and Smart Structures for Industry 4.0”.

Received 15 June 2023  
Revised 20 October 2023  
15 March 2024  
Accepted 18 March 2024

---

The current issue and full text archive of this journal is available on Emerald Insight at: <https://www.emerald.com/insight/1355-2546.htm>



Rapid Prototyping Journal  
30/11 (2024) 123–141  
Emerald Publishing Limited [ISSN 1355-2546]  
[DOI 10.1108/RPJ-06-2023-0194]

metal components using the FFF technology [metal FFF (MFFF)]. The raw material is a filament containing metal powders (up to 90 wt.%) embedded into a polymeric matrix (Figure SI.1 of the Supplementary Information). After the printing process, the so-called “green part” undergoes first debinding to partially remove the polymeric binder, obtaining the “brown part” (BASF, 2022; Liu *et al.*, 2020; Wagner *et al.*, 2022), and then sintering to remove the secondary polymer and create a solid metal object (BASF, 2022; Jiang and Ning, 2022a; Wagner *et al.*, 2022).

Many MFFF filaments are currently available or under development, demonstrating the growing scientific and industrial interest in this field. According to Suwanpreecha and Manonukul (2022), 316L stainless steel is the most used and studied material, followed by 17-PH stainless steel, Ti-6Al-4V alloy and Cu. 316L stainless steel is characterised by a valuable combination of properties, including high corrosion and mechanical resistance, good ductility, and biocompatibility. It is an ideal material for applications in several fields, such as biomedical or aerospace (Caminero *et al.*, 2021). Over one-third of the studies use the commercial 316L feedstock from BASF (Suwanpreecha and Manonukul, 2022), named Ultrafuse 316L (UF316L) (BASF, 2021, 2022). However, there are also works in literature focused on in-house 316L filaments (Thompson *et al.*, 2019; Wagner *et al.*, 2022); in these works, in addition to printing parameters, aspects concerning the filament fabrication, the selection of the size of the metallic powder, its volumetric percentage, and the binder and additives used to ensure extrudability are discussed. All these aspects were reviewed in Bankapalli *et al.* (2023).

Table 1 summarises the main results in the literature concerning printing, debinding and sintering (“D&S”) parameters of samples/components fabricated with the UF316L filament. Specifically, the studies reported in Table 1 analyse the influence of printing parameters, build orientation, and “D&S” protocols on mechanical properties, shrinkage, porosity, and microstructure. Different methods, such as microstructural analysis by optical and scanning electron microscope (SEM), dimensional and hardness measurements, and tensile testing, are used to investigate material properties. From Table 1, the following considerations can be derived:

- Microstructure and mechanical properties are affected by printing parameters (Damon *et al.*, 2019; Gong *et al.*, 2018, 2019; Kasha *et al.*, 2022; Moritzer *et al.*, 2021; Quarto *et al.*, 2021) and build orientation (Ait-Mansour *et al.*, 2020; Caminero *et al.*, 2021, 2022; Damon *et al.*, 2019; Pellegrini *et al.*, 2022).
- During D&S, parts undergo an anisotropic shrinkage of about 15%–20% in the printing plane ( $x$ - $y$ ) and 18%–25% along the printing direction ( $z$ ) (Ait-Mansour *et al.*, 2020; Caminero *et al.*, 2021, 2022; Gong *et al.*, 2018, 2019; Liu *et al.*, 2020; Obadimu and Kourousis, 2022a; Quarto *et al.*, 2021; Rosnitschek *et al.*, 2021; Tosto *et al.*, 2021); shrinkage is influenced by printing parameters, such as layer height and raster angle (Obadimu and Kourousis, 2022a), build orientation (Caminero *et al.*, 2021), and printing speed (Quarto *et al.*, 2021).
- Build orientation and printing strategy strongly influence the pore architecture (Damon *et al.*, 2019); it is possible to distinguish between a manufacturing-induced porosity and a

- D&S porosity, with the first dominating over the second (Caminero *et al.*, 2022; Damon *et al.*, 2019; Liu *et al.*, 2020).
- Sintered parts are characterised by strain-free equiaxed grains with twins; grain morphology is not dependent on the build orientation (Caminero *et al.*, 2021, 2022; Damon *et al.*, 2019; Gong *et al.*, 2018, 2019; Liu *et al.*, 2020).
- Tensile testing reveals that even when printing is optimised to obtain a near fully dense part, mechanical properties (ultimate tensile strength (UTS), elongation at break and yield strength) are lower than those of 316L steel produced by metal injection moulding (MIM) and laser powder bed fusion (LPBF) (Caminero *et al.*, 2021, 2022; Gong *et al.*, 2018, 2019; Moritzer *et al.*, 2021; Obadimu *et al.*, 2022; Rosnitschek *et al.*, 2021; Tosto *et al.*, 2021). Consistently, the hardness of the MFFF 316L is lower than that of the same material produced by LPBF (Gong *et al.*, 2018, 2019).
- Surface roughness is affected by the printing parameters, build orientation, and deposition angle, i.e., the angle between the building direction and the normal to the surface to be evaluated (Boschetto *et al.*, 2022; Caminero *et al.*, 2022).

This overview underlines how much printing parameters influence samples’ microstructure and mechanical properties. Besides, these properties are lower than those obtainable through more consolidated manufacturing processes such as MIM and LPBF. The MFFF technology also introduces further variabilities compared to LPBF, related to the debinding and sintering phases necessary after printing. Therefore, further deepening this influence is essential to strengthening the role of MFFF technology in metal AM. For example, in those studies, density and porosity analyses are performed on the sintered specimens, whereas investigations on the green state are limited. That is an important underlining limitation because the manufacturing-induced porosity of MFFF 3D-printed components is also strictly related to the printing path. Moreover, performing these analyses on not sintered samples allows testing several variables and configurations with limited costs, as green parts can potentially be recycled, as recently demonstrated in Bocchi *et al.* (2024). Therefore, this investigation can also be anticipated at the green state to collect further potentially relevant insights.

Together with printing parameters, it is also necessary to provide design for additive manufacturing (DfAM) guidelines to drive the dimensioning of the parts and fully exploit the MFFF design potential. Numerous works focus on elaborating FFF design guidelines with thermoplastic polymers (e.g., Guerra Silva *et al.*, 2021; Medellin-Castillo and Zaragoza-Siqueiros, 2019; Steuben *et al.*, 2015); little has been done regarding DfAM guidelines for MFFF components, including how the D&S process affects the outcomes of the fabrication process. Even if printed successfully, as binders are removed, parts could lack structural integrity and experience collapse or distortion under their weight. A valuable contribution to this topic is provided in Jiang and Ning (2022a), where the shrinkage and deflection ratio of overhang pillars characterised by different overhang angles are analysed. Through an integrated approach that combines analytical modelling, finite element simulation, and experimental validation, the authors found that overhang angles directly influence the shrinkage of a single inclined strut. Although this

Table 1 Process parameters available in the literature for the UF316L filament

| Parameter/source                          | (Caminero et al., 2021) | (Gong et al., 2018, 2019) | (Damon et al., 2019) | (Liu et al., 2020)      | (Jimbo and Tateno, 2019) | (Tosto et al., 2021) | (Jiang and Ning, 2021, 2022a) | (Carminati et al., 2021; Quarto et al., 2021) | (Rosnitschek et al., 2021) | (Moritzer et al., 2021) | (Ait-Mansour et al., 2020) | (Obadimu et al., 2022; Obadimu and Kourousis, 2022a) |
|---|-------------------------|---------------------------|----------------------|-------------------------|--------------------------|----------------------|-------------------------------|---|----------------------------|-------------------------|----------------------------|--|
| Metal composition [%]                     | Ultimaker 3             | Flashforge Dreamer        | Apium P155           | metal 3D printer ColiDo | Axiom Dual, Airwolf      | Zortrax M200         | Lulzbot Taz6                  | Ultimaker S5                                  | German RepRap X500         | Prusa i3 MK3s           | Funmat HT                  | Prusa i3MK3  |
| Nozzle diameter [mm]                      | 0.6                     | 0.4                       | 0.4                  | /                       | 0.4                      | 0.4                  | 0.5                           | 0.6   | 0.4                        | 0.25, 0.4               | 0.4                        | 0.4  |
| Layer height [mm]                         | 0.1                     | 0.2                       | 0.1                  | 0.2                     | 0.22                     | 0.14                 | 0.2                           | 0.1, 0.4                                      | 0.2                        | 0.125, 0.2              | 0.2                        | 0.15, 0.20, 0.25                                     |
| Line width related to nozzle diameter [%] | 0.56                    | /                         | 0.48                 | /                       | /                        | /                    | /                             | /   | 0.5                        | 87.5, 120, 152.5%       | 0.4                        | 0.4  |
| Infill [%]                                | 100                     | /                         | 100                  | 100                     | /                        | 100                  | 100                           | 100   | 25, 50, 75, 100            | 100                     | 25, 50, 75, 100, 125       | 100  |
| Infill type                               | Catalytic + thermal     | Catalytic                 | Catalytic + thermal  | Catalytic + thermal     | Thermal                  | Catalytic            | Catalytic + thermal           | Catalytic + thermal                           | Catalytic + thermal        | /                       | Catalytic + thermal        | Catalytic + thermal                                  |
| Print temp. [°C]                          | 230                     | 235                       | 210                  | Lines 230               | 240                      | 240                  | Lines 240                     | Lines/concentric 170, 240                     | Hexagonal 240              | Lines 230               | Lines 235                  | Lines 235  |
| Bed temp. [°C]                            | 100                     | /                         | 120                  | /                       | /                        | 90                   | 100                           | 100   | 90, 120, 140               | 120                     | 90                         | 90   |
| Print speed [mm/s]                        | 15                      | 60                        | 33                   | /                       | 35                       | /                    | 30                            | 20, 50  | 25                         | 20, 25, 34              | 30                         | 30, 35, 40   |
| Debinding                                 | Pure H atm.             | Catalytic                 | Catalytic + thermal  | Catalytic + thermal     | Thermal                  | Catalytic            | Catalytic + thermal           | Catalytic + thermal                           | Catalytic + thermal        | /                       | Catalytic + thermal        | Catalytic + thermal                                  |
| Sintering                                 | Pure H atm.             | Pure H atm. or vacuum     | Pure H atm.          | Argon atm.              | Vacuum                   | H atm.               | Pure H atm                    | Argon atm                                     | Pure H atm                 | /                       | Argon atm                  | Pure H atm   |
| Porosity (as-sintered) [%]                | 1.9–2.1                 | 1.5                       | 0.5–1.7              | 7.7                     | /                        | 9.8                  | 4.4                           | 5   | 11.4 (for 100% infill)     | /                       | 4.6 (for 100% infill)      | /  |

Notes: Underlined parameters are those considered optimal by the study's authors. When details are unavailable in the cited study, the "/" symbol is used

Source: Table created by the authors with data from the cited works

study provides valuable guidance for designing metallic complex morphologies with overhangs, further research is needed to demonstrate the possibility of adopting MFFF to produce more challenging morphologies. Additional findings are provided in the study of Shaikh *et al.* (2021a), where the deflection of unsupported horizontal beams was found to be dependent on both their length and cross-sectional shape.

Hence, the contribution of this study is threefold. Firstly, it further deepens the analysis of the influence of printing parameters on the structural and mechanical properties of MFFF 316L parts, also considering the green state. Secondly, it derives DfAM rules providing considerations related to the printing and the D&S phases. Third, it demonstrates the possibility of extending the range of complex morphologies printable using MFFF. So far, few studies on lattice structures produced via MFFF are available in the literature. Some examples are discussed in Shaikh *et al.* (2021a) and Jiang and Ning (2022b) for Ti6Al4V and 17–4 PH grade stainless steel filaments, respectively. Concerning the 316L stainless steel, i.e., the material analysed in this study, examples of MFFF-fabricated samples are presented in Wagner *et al.* (2022) and Obadimu and Kourousis (2022b). Wagner and co-workers developed a new binder system and produced a filament with a metal load of about 50% (significantly lower than the one of the UF316L used in the present work). That filament was used to print face-centred cubic (FCC) plate-lattice arrays (Wagner *et al.*, 2022). Obadimu and Kourousis successfully manufactured honeycomb lattices using the UF316L filament and analysed their compressive behaviour (Obadimu and Kourousis, 2022b). Hence, considering the growing interest in cellular structure design and the limited studies focusing on MFFF as their manufacturing process, the paper aims to address this further knowledge gap. To this aim, strut-and-node and triply periodic minimal surface (TPMS)

lattices with constant or graded relative density were printed, debinded, and sintered.

2. Materials and methods

Samples were printed using the Ultimaker S5 (Ultimaker, 2022a) printer, the Red Printcore CC nozzles with 0.6 mm and 0.4 mm diameters and the UF316L filament from BASF that contains 90 wt.% of metal powder (BASF, 2022). The Ultimaker Cura 4.11 was used as slicer software. An oversizing factor of 120% in the bed plane directions and 126% in the print one was applied to all prints. Concerning the D&S steps, the guidelines and steps suggested for the UF316L filament were followed. They include catalytic debinding at 120°C in an atmosphere with HNO<sub>3</sub> > 98%, heating from room temperature up to 600°C with a ramp of 5°C/min, soaking at 600°C for 1 h, heating from 600°C up to 1,380°C with a ramp of 5°C/min; soaking for 3 h at 1,380°C and furnace cooling. Sintering was performed in a full hydrogen atmosphere (BASF, 2022).





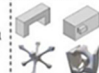
An overview of the experimental procedure of the study is shown in Figure 1. Three main phases can be identified (Figure 1 top row, from left to right):

- analysis of the printing parameters;
- characterisation of the sintered parts; and
- investigation of manufacturability limits.

2.1 Analysis of the printing parameters

Printing parameters can be divided into two groups: “process” and “toolpath” (Turner and Gold, 2015). The firsts determine the success of the print. Once process parameters are fixed, the toolpath ones can be modified: they influence how the material is distributed within the design space and, thus, the parts’ density and mechanical properties.

Figure 1 Overview of the study workflow

|            | Analysis of the printing parameters (Section 2.1)   |   |  | Characterization of the sintered parts (Section 2.2)  |  | Investigation of the manufacturability limits (Section 2.3)                           |  |
|------------|---|---|--|---|--|---|--|
|            | Process parameters analysis   | Toolpath parameters analysis  |  | Density and porosity investigation  | Tensile testing  | Printability assessment   |  |
| Samples    | 10 mm cube   | Prism with square base (10x10x5mm <sup>3</sup> )   |  |    |    |  |  |
| Parameters | <ul style="list-style-type: none"> <li>• Layer height</li> <li>• Line width</li> <li>• Print temperature</li> <li>• Bed temperature</li> <li>• Flow</li> <li>• Print speed</li> <li>• Plate adhesion</li> </ul> | <b>1° step</b> <ul style="list-style-type: none"> <li>• Infill type</li> <li>• Wall line count</li> <li>• Infill overlap</li> </ul>   | <b>2° step</b> <ul style="list-style-type: none"> <li>• Infill density</li> </ul>  | <b>3° step</b> <ul style="list-style-type: none"> <li>• Infill type</li> <li>• Wall line count</li> </ul>                           | <ul style="list-style-type: none"> <li>• Infill type</li> <li>• Wall line count</li> <li>• Infill overlap</li> <li>• Infill density</li> </ul>       | <ul style="list-style-type: none"> <li>• MIM vs FFF</li> <li>• Infill type</li> </ul> | <ul style="list-style-type: none"> <li>• Bridges</li> <li>• Horizontal holes</li> <li>• Unsupported edges</li> <li>• Overhang angles</li> <li>• Type of lattice</li> <li>• Relative density</li> </ul> |
| Objective  | <ul style="list-style-type: none"> <li>• Identification of the best printing set of parameters</li> </ul>   | <ul style="list-style-type: none"> <li>• Internal porosity evaluation</li> <li>• Evaluation of the lateral surface quality</li> </ul> | <ul style="list-style-type: none"> <li>• Internal porosity evaluation</li> <li>• Evaluation of the lateral surface quality</li> <li>• Over-extrusion quantification</li> </ul> | <ul style="list-style-type: none"> <li>• Evaluation of the dimensional accuracy</li> <li>• Over-extrusion quantification</li> </ul> | <ul style="list-style-type: none"> <li>• Density measure</li> <li>• Apparent porosity calculation</li> <li>• Internal porosity evaluation</li> </ul> | <ul style="list-style-type: none"> <li>• Mechanical characterisation</li> </ul>       | <ul style="list-style-type: none"> <li>• Printability and D&amp;S feasibility evaluation</li> </ul>  |
| Analysis   | <ul style="list-style-type: none"> <li>• Visual inspection</li> </ul>   | <ul style="list-style-type: none"> <li>• ImageJ analysis</li> <li>• Visual inspection</li> </ul>                                      | <ul style="list-style-type: none"> <li>• ImageJ analysis</li> <li>• Visual inspection</li> <li>• Weight</li> </ul>   | <ul style="list-style-type: none"> <li>• Visual inspection</li> <li>• Dimensions measurement</li> <li>• Weight</li> </ul>           | <ul style="list-style-type: none"> <li>• Hydrostatic balance</li> <li>• LOM imaging</li> </ul>   | <ul style="list-style-type: none"> <li>• Tensile test</li> </ul>                      | <ul style="list-style-type: none"> <li>• Visual inspection</li> </ul>  |

**Notes:** For each main phase of the study, the following details are summarised: the sample used, the parameters analysed, the targets of the analysis and the type of analysis performed. A reference to the paper’s Sections is also provided. A comparison with Metal Injection Moulded (MIM) samples has also been included

**Source:** Figure by authors

### 2.1.1 Process parameters analysis

The first step focused on investigating the effect of process parameters on the formation of visible defects. Being such parameters responsible for the success of the printing process, only visual inspection of the printed samples was performed at this stage (Figure 1, “Analysis” row). Based on it, samples were classified either as successfully printed or failed. A successfully printed sample is obtained when there is no detachment from the substrate, deformation, cracking, or delamination of the part and nozzle clogging, or any other printer setup failures or damages have occurred. Three printing profiles (A0, B0, and C) and their variations were investigated (see Table 2).

Set A0 was designed after preliminary tests (see Section SI.2 of the Supplementary Information, Table SI.2 and Figure SI.4). Set B0 was derived from the study of Caminero *et al.* (2021) because they used the Ultimaker 3 printer (which is similar to the system used in our study) and the Cura slicer software (same for this study). Besides, their printing parameters are close to the values suggested by BASF (2022), reaching a porosity level of 1.90% (Table 1). For both Set A0 and B0, the infill density is 100%. The infill pattern is *Lines* for Set A0 and *Concentric* for Set B0. Set C is the combination of parameters indicated by Cura for the UF316L. It is worth explaining that this set of parameters was made available in the Cura software when the experimental study was already started. The infill density is 105%, while the infill pattern is *Lines*. Starting from the baseline profiles A0 and B0, some changes were implemented by modifying one parameter at a time, as shown in Table 2, to obtain additional printing profiles (A1 ÷ A5, B1 ÷ B5). No changes were implemented on Set C. The raster angle of the *Lines* infill is  $\pm 67^\circ$ .

In the A1 and B1 sets, the print speed was raised and lowered. A2 and B2 were used to study the adhesion of the parts on the build plate by changing the adhesion type. Layer height was modified in the A3 and B3 sets. The A4, A5, B4, and B5 sets were used to explore the influence of printing and bed temperatures. The line width and flow parameters were kept constant.

The specimen geometry was a  $10 \times 10 \times 10 \text{ mm}^3$  cube (Figure 1, “Samples” row). Three replicas for each profile were printed.

**Table 2** Printing parameters of the analysed profiles (A0 ÷ A5, B0 ÷ B5, C)

| Parameter              | Sets A |           |             |            |            |           | Sets B     |          |             |            |            |           | Set C |
|------------------------|--------|-----------|-------------|------------|------------|-----------|------------|----------|-------------|------------|------------|-----------|-------|
|                        | A0     | A1        | A2          | A3         | A4         | A5        | B0         | B1       | B2          | B3         | B4         | B5        | C     |
| Layer height [mm]      | 0.2    | 0.2       | 0.2         | <b>0.1</b> | 0.2        | 0.2       | 0.1        | 0.1      | 0.1         | <b>0.2</b> | 0.1        | 0.1       | 0.2   |
| Line width [mm]        | 0.6    |           |             |            |            |           | 0.56       |          |             |            |            |           | 0.6   |
| Print temperature [°C] | 240    | 240       | 240         | 240        | <b>230</b> | 240       | 230        | 230      | 230         | 230        | <b>240</b> | 230       | 240   |
| Bed temperature [°C]   | 80     | 80        | 80          | 80         | 80         | <b>90</b> | 100        | 100      | 100         | 100        | 100        | <b>90</b> | 100   |
| Flow [%]               | 104    |           |             |            |            |           | 100        |          |             |            |            |           | 100   |
| Print speed [mm/s]     | 7      | <b>20</b> | 7           | 7          | 7          | 7         | 15         | <b>7</b> | 15          | 15         | 15         | 15        | 25    |
| Plate adhesion type    | brim   | brim      | <b>raft</b> | brim       | brim       | brim      | brim       | brim     | <b>raft</b> | brim       | brim       | brim      | brim  |
| Infill type            | Lines  |           |             |            |            |           | Concentric |          |             |            |            |           | Lines |
| Infill [%]             | 100    |           |             |            |            |           | 100        |          |             |            |            |           | 105   |

**Note:** In sets A and B, the variations from the reference profile (A0 and B0, respectively) are highlighted in bold

**Source:** Table by authors

The set of parameters considered the best was selected for the rest of the study.

### 2.1.2 Toolpath parameters analysis

After analysing the process parameters, the toolpath parameters were assessed to understand their influence on the sample porosity. The specimen geometry was a prism with a square face of  $10 \times 10 \text{ mm}^2$  and a height of 5 mm (Figure 1, “Samples” row). The samples were printed without the top layers to investigate their internal porosity. Three replicas for each configuration of parameters were printed. This study phase was conceived to be structured into three steps (Figure 1, “Parameters” row).

In the first step, the analysed parameters were:

- *Infill type*: Lines, Zig-zag, and Concentric.
- Wall line count: 0, 1, and 3.
- Infill overlap (Ov), i.e., the overlap between the infill and the first wall line: 0.19 (the default value in Cura 4.11) and 0.28 mm. The overlap distance is measured along the deposition direction, considering the centre of the nozzle. The rounded end of the deposited lines implies the “addition” of a distance equal to almost half of the line width (W/2) (Figure 2).

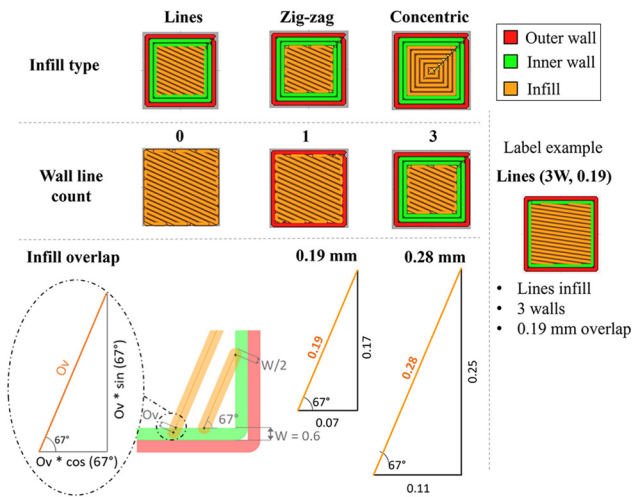
Specimens were named according to their infill type, number of wall lines, and amount of overlap. For example, the sample labelled as “Lines (3W, 0.19)” has the following characteristics: the infill type is *Lines*, three wall lines were printed, and the overlap is 0.19 mm (Figure 2).

In the case of the concentric infill type, the infill never overlaps the wall. Thus, we considered the following samples:

- Concentric (10): the wall line count is 3, and the sample cross-section dimension is 10 mm.
- Concentric (10; 45°): it is equal to Concentric (10) but printed rotated at 45° (Figure SI.3, Supplementary Information).
- Concentric (12): it is a prism with a cross-section of  $12 \times 12 \text{ mm}^2$  and a height of 4 mm. The specimen dimensions were modified to make them a multiple of the line width (i.e., 0.6 mm).

In addition to the visual inspection of the samples, the porosity value was estimated from sample pictures (Figure 1, “Analysis”

**Figure 2** The investigated toolpath parameters: infill type (*Lines*, *Zig-zag*, and *Concentric*), wall line count (0, 1, and 3), and infill overlap (0.19 and 0.28 mm)



**Notes:** Both outer and inner walls are considered in the wall line count. At the bottom right is an example of how samples were labelled. Ov = overlap; W = line width

**Source:** Figure by authors, inspired by Ultimaker, (2022b)

row) using the ImageJ software by converting the photos of the last layer of the samples into a white/black format (see Figure SL2, Supplementary Information). Being the portions covered by the material coloured in white in the resulting image, the porosity was calculated as the percentage of black pixels inside the selected region.

The second step concerns the infill density (Figure 1, “Parameters” row). By increasing it to values above 100%, the deposited lines start to overlap, theoretically reducing the possible gaps between them. This causes an over-extrusion condition. In addition to 105% infill, three other values were considered: 120%, 135%, and 150%. The selected printing profile was *Lines* (0 W).

In addition to the analyses performed in the previous step (visual inspection and ImageJ analysis), the weight of each sample was measured at this stage by using a precision digital weight scale (Kern PCB 2500–2, 0.01 g resolution) (Figure 1, “Analysis” row) to quantify the weight increase due to the over-extrusion condition.

The third step was focused on understanding how the selection of the parameters influences the dimensional accuracy of the green part printed at high infill density (Figure 1, “Parameters” row). Four profiles were tested: 120%\_Lines (0 W), 120%\_Lines (1 W, 0.19), 120%\_Zig-zag (0 W) and 120%\_Zig-zag (1 W, 0.19). The 120% infill density was selected because, as discussed later, this value resulted in no visible porosity and no sign of over-extrusion. In this step, the following analyses were performed (Figure 1, “Analysis” row): visual inspection, weighing (precision digital scale), and dimensional measurements with a micrometre screw gauge.

## 2.2 Characterisation of the sintered parts

### 2.2.1 Metal specimens’ density and porosity investigation

Selected specimens were debinded and sintered. The density of the metal parts was measured through Archimedes’ method

and compared with the nominal density of the bulk material ( $8.0 \text{ g/cm}^3$ ) to calculate the apparent porosity. This value was obtained as:  $\left(\frac{\rho_{th} - \rho_{sample}}{\rho_{th}}\right) * 100$ , where  $\rho_{th}$  is the nominal density of the 316L stainless steel. Additionally, the microstructure of the samples was analysed. One specimen for each type was cut, embedded into epoxy resin and polished with abrasive papers and diamond pastes. Light optical microscopy (LOM) was used to inspect the internal pores and their distribution within the parts (Figure 1, “Analysis” row).

### 2.2.2 Tensile testing of MFFF and MIM samples and microstructural analysis

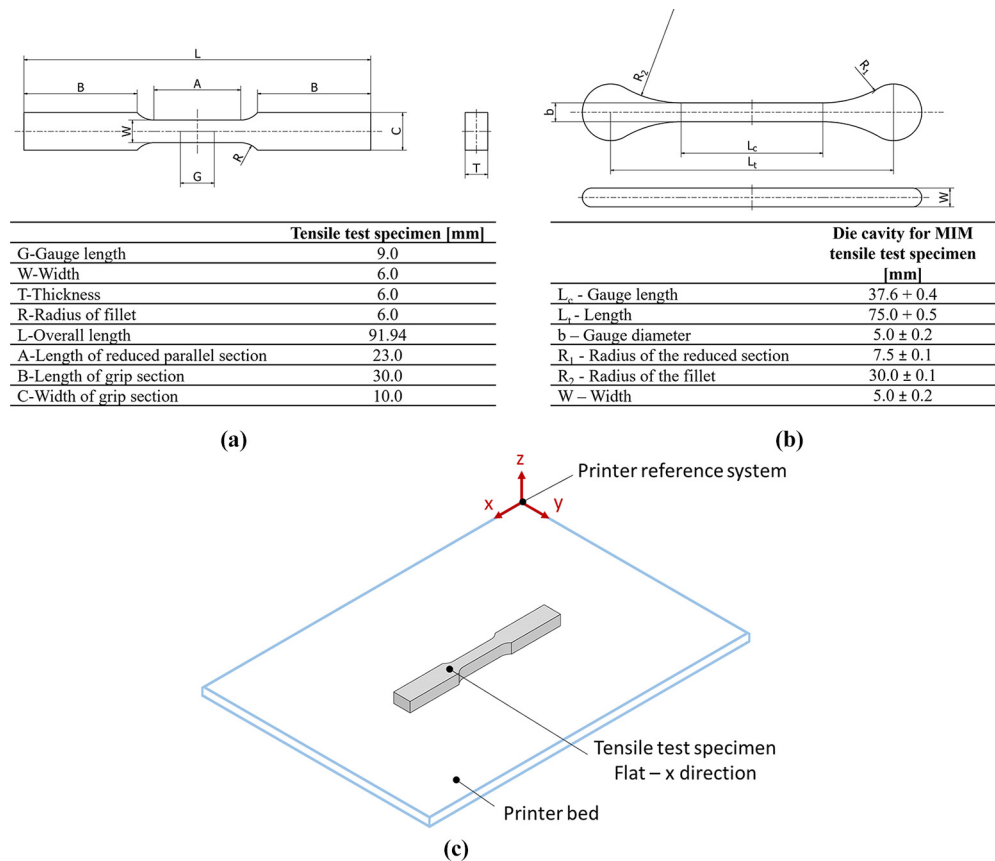
After defining the optimal printing set for the UF316L, tensile tests were conducted to evaluate the mechanical properties of printed parts (Figure 1, “Analysis” row). 316L MIM specimens were also tested for the sake of comparison. The tested specimens are a modified version of the *Rectangular Subsize Specimen* described by the ASTM E8/E8M standard (ASTM, 2020). Dimensions were reduced to lower the material required during printing [Figure 3(a)].

Two types of tensile test specimens were printed with different structural parameters: one wall (1 W), 105% infill density and two infill patterns (i.e., *Lines* and *Zig-zag*, see also Figure 2). These specimens were named “Tensile Specimens Lines” and “Tensile Specimens Zig-zag”. The tensile test specimens were printed flat, as shown in Figure 3(c). In the literature, typically, three orientations have been studied, i.e., flat, on-edge, and vertical. All the available studies and the technical data sheet of the UF316L (BASF, 2021) report that the vertical orientation exhibits the lowest tensile properties due to layer delamination (Suwanpreecha and Manonukul, 2022). On the other hand, the difference between the flat and on-edge orientation is still inconsistent (Suwanpreecha and Manonukul, 2022). The studies of Caminero *et al.* (2021, 2022), Pellegrini *et al.* (2022) and Damon *et al.* (2019) reported no significant difference between these two orientations. Therefore, the flat orientation was chosen. Three replicas were printed for each type. Three 316L specimens produced with the MIM technology were also tested [Figure 3(b)] (ISO, 2009). Before testing, the specimens were subjected to solution annealing. The lateral surfaces were machined to guarantee a smooth surface. The electro-mechanical testing machines MTS Alliance RT/100 and MTS Alliance RF 150 were used for the tensile testing. Tensile tests were performed according to the ASTM E8/E8M standard at room temperature, under a constant crosshead speed of 0.5 mm/min.

Images of the fracture surfaces and the microstructure of the specimens were taken and analysed by using multiple microscopy techniques. In particular, microstructural analysis was performed on the grip side of the specimens. Samples were etched with water, hydrochloric acid, and nitric acid solution mixed in equal proportions. Samples were immersed in this solution for 30–40 s and then washed and dried. This operation was done to reveal the grain structure of the steel. The Nikon EclipseLV150NL optical microscope and the Zeiss Evo 50 SEM were used for the metallographic analysis.

### 2.3 Investigation of the manufacturability limits

To test the suitability of the printing parameters, four recurring geometries were selected: bridges, horizontal holes, unsupported

**Figure 3** Dimensions and printing orientation of the tensile test specimens

**Notes:** (a) Dimensions of the tensile test specimen used in this study; (b) dimensions of the MIM tensile test specimen according to the ISO 2740 standard (ISO, 2009); (c) Printing orientation of the tensile test specimens

**Source:** Figure by authors

edges, and overhang angles. These are some of the most popular geometries among those usually mentioned in the so-called “design rules for additive manufacturing”, as they derive from the physical limits of the used technology. These features, designed based on the indications provided in HUBS(2022) and Hydra Research 3D (2022), are shown in Figure 4(a)–(d).

Bridges are horizontal beams suspended in mid-air. Four lengths were tested: 5, 10, 15, and 20 mm [Figure 4(a)], with 10 mm representing a reference value. We tested horizontal holes with four different geometries [Figure 4(b)]: a circular hole, a droplet hole, an elliptic hole, and a “complex” hole. We tested three overhang angles: 45°, 40°, and 35° [Figure 4(c)]. Reference values of 45° or 40° (i.e., 50° if measured from the vertical axis) can usually be found. Unsupported edges are features printed mid-air without supports. The dimensions of the features were set as a multiple of the extrusion width: 0.6, 1.2, 1.8, and 2.4 mm [Figure 4(d)]. The maximum reference value for these features is two times the extrusion width. Then, some lattice structures, shown in Figure 5, were also printed. The Supplementary Information (Table SI.1) contains additional details about these lattices. The software *Functional Lattice Package (Flatt Pack)* was used (Maskery et al., 2022) to generate their geometry. These samples were then printed

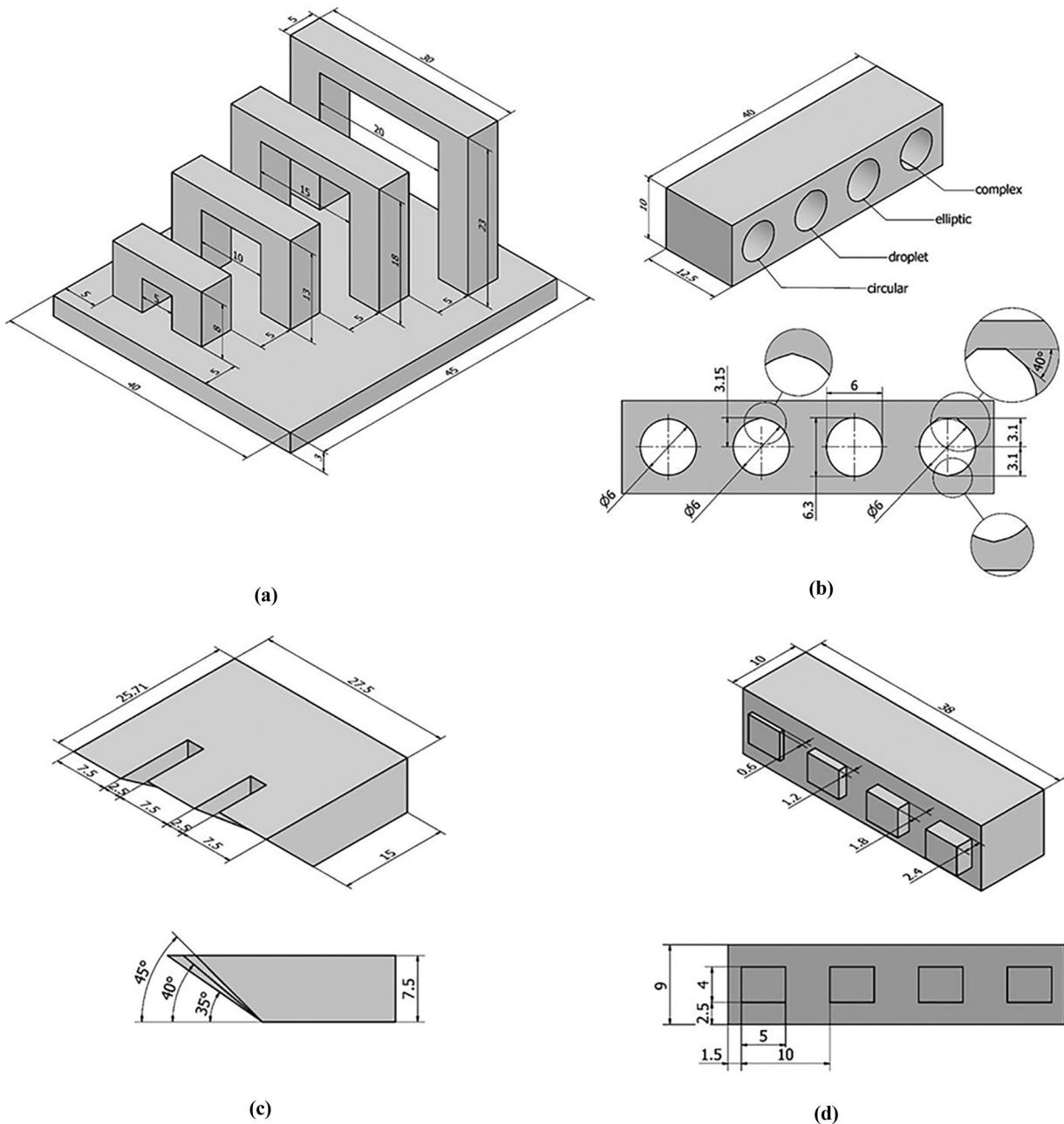
using the default parameters for the UF316L filament (“C” profile, Table 2), with a line width equal to the diameter of the selected nozzle. When specified, polyvinyl alcohol (PVA) was used as support material. The Supplementary Information (Figure SI.5) shows further examples of printed arrays and unit cells created for running the preliminary analysis of the printing parameters.

### 3. Results and discussion

#### 3.1 Analysis of the printing parameters

##### 3.1.1 Process parameters analysis

The results of the analysis of the process parameters are shown in Figure 6. The obtained results are consistent in sample replicas. The A0 and B0 sets lead to successful prints. No noticeable differences were detected in A1 when the speed was increased. In the case of B1, the edges of the parts started rising from the surface, leading to distortions in the first layers. The part started detaching during the printing of the last layers. Specimen B1 detached from the plate quite early. The printing times of A1 and B1 were 14 and 23 min, respectively, comparable to those of A0 (13 min) and B0 (25 min). The print speed does not significantly influence the printing time in small

**Figure 4** CAD models of the selected features to be 3D-printed

**Notes:** (a) Bridges (5 mm, 10 mm, 15 mm, and 20 mm); (b) horizontal holes (circular, droplet, elliptic and complex hole geometry); (c) overhang angle (35°, 40°, and 45°); (d) unsupported edges (0.6mm, 1.2mm, 1.8mm, 2.4 mm)

**Source:** Figure by authors

parts. Nevertheless, a low print speed could lead to problems of adhesion and detachment.

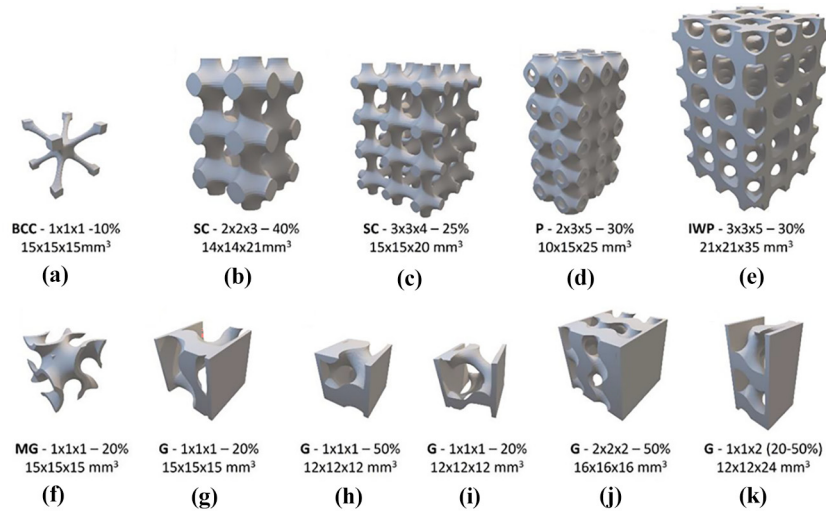
For adhesion purposes, all the specimens were printed with a brim structure and a thin coat of hairspray on the glass substrate of the machine. A2 and B2 changed the adhesion structure to raft with poor outcomes. The bottom layers started shrinking and detaching on one side during printing, lifting the parts and pushing them against the nozzle. The raft structure had also been difficult to remove

without creating any damage at the bottom of the specimens.

The parts with a variation in layer height were A3 (i.e., 0.1 mm) and B3 (i.e., 0.2 mm). A higher layer height leads to a rougher surface, and the layers can be distinguished more easily. In the case of B3, the prints failed because of the detachment of the first layer from the bed. This could be attributed to the steeper gradients formed in the B3 sample leading to higher stresses.



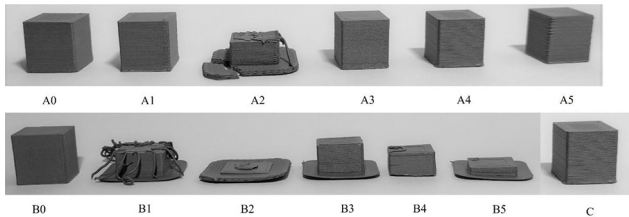
**Figure 5** Examples of the 3D-printed lattices



**Notes:** Array, relative density, and final dimensions are reported for each structure or unit cell. (a) A BCC unit cell; (b) A 2x2x3 SC structure; (c) A 3x3x4 SC structure; (d) A 2x3x5 matrix-based Primitive structure; (e) A 3x3x5 network-based IWP structure; (f) A matrix-based Gyroid unit cell; (g) A network-based Gyroid unit cell with lateral walls. (h) A network-based Gyroid unit cell with lateral walls (50% volume fraction); (i) A network-based Gyroid unit cell with lateral walls (20% volume fraction); (j) A 2x2x2 network-based Gyroid structure; (k) A 1x1x2 network-based Gyroid structure with a linear volume fraction gradient

**Source:** Figure by authors

**Figure 6** Results of the process parameters analysis. One specimen from every set A, B and C is shown



**Note:** The sample used for this analysis is a 10 mm cube

**Source:** Figure by authors

A4, B4, A5, and B5 had variations in the printing and bed temperatures (Table 2). The A-based profiles were always successfully printed. The B-based profiles experienced adhesion problems that can be attributed to the combination of two effects. Firstly, a higher nozzle temperature (e.g., in B4) and a lower bed temperature (e.g., in B5) lead to steeper thermal gradients than sample B0. Secondly, the line width smaller than the nozzle size used for every B set meant that less material was extruded per unit volume, leading to higher thermal stresses. A was the most reliable for printing when comparing A and B profiles. Indeed, apart from changing the adhesion structure from brim to raft, none of the other variations compromised the success of the print. However, both sets suffer from nozzle clogging. Finally, all the prints performed with the C profile were successful, without any sign

of clogging or adhesion problems. Therefore, C was the set used for all the following jobs except where otherwise specified.

### 3.1.2 Toolpath parameters analysis

Once the process parameters were defined, specimens were printed with different combinations of toolpath parameters (Figure 2). The density results are reported in Table 3. Each

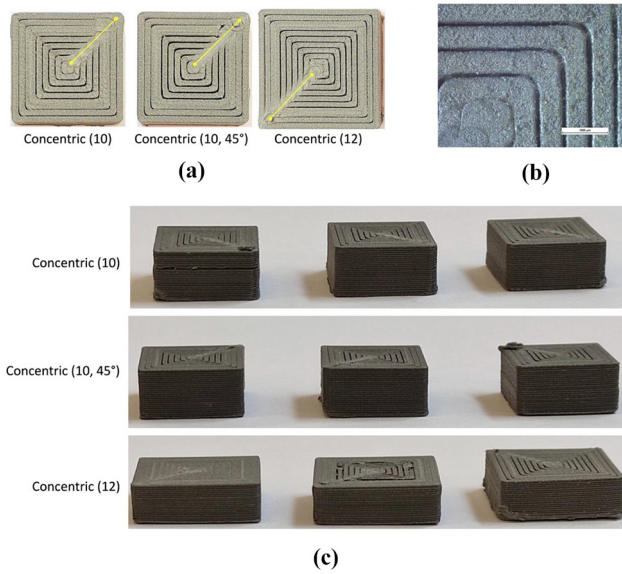
**Table 3** Density (mean  $\pm$  standard deviation) and porosity of the samples printed to analyse the influence of toolpath parameters (infill type, wall line count, and infill overlap)

| Specimen                  | Density ( $\mu \pm \sigma$ ) [%] | Porosity [%] |
|---------------------------|----------------------------------|--------------|
| 105%_Concentric (10)      | 93.11 $\pm$ 1.66                 | 6.89         |
| 105%_Concentric (10; 45°) | 91.65 $\pm$ 0.76                 | 8.35         |
| 105%_Concentric (12)      | 92.96 $\pm$ 5.35                 | 7.04         |
| 105%_Lines (3W, 0.19)     | 95.63 $\pm$ 2.87                 | 4.37         |
| 105%_Lines (3W, 0.28)     | 99.17 $\pm$ 0.86                 | 0.83         |
| 105%_Lines (1W, 0.19)     | 99.07 $\pm$ 1.14                 | 0.93         |
| 105%_Lines (1W, 0.28)     | 99.80 $\pm$ 0.26                 | 0.20         |
| 105%_Lines (0W)           | 90.32 $\pm$ 0.20                 | 9.68         |
| 105%_Zig-zag (3W, 0.19)   | 93.64 $\pm$ 1.42                 | 6.36         |
| 105%_Zig-zag (3W, 0.28)   | 97.96 $\pm$ 0.99                 | 2.04         |
| 105%_Zig-zag (1W, 0.19)   | 93.64 $\pm$ 1.35                 | 6.36         |
| 105%_Zig-zag (1W, 0.28)   | 96.94 $\pm$ 1.14                 | 3.06         |
| 105%_Zig-zag (0W)         | 95.72 $\pm$ 2.85                 | 4.28         |

**Notes:** For the sample labelling, see Figure 2. All samples were printed with the C profile, thus with a 105% infill (Table 2)

**Source:** Table by authors

**Figure 7** Concentric infill



**Note:** (a) Picture of one specimen for each toolpath parameters combination. The sign of the beginning of the printing lines is highlighted in yellow; (b) optical microscope image of the most recurrent defect, that is, the presence of gaps between the printing lines; (c) all the printed specimens with a focus on their external surfaces

**Source:** Figure by authors

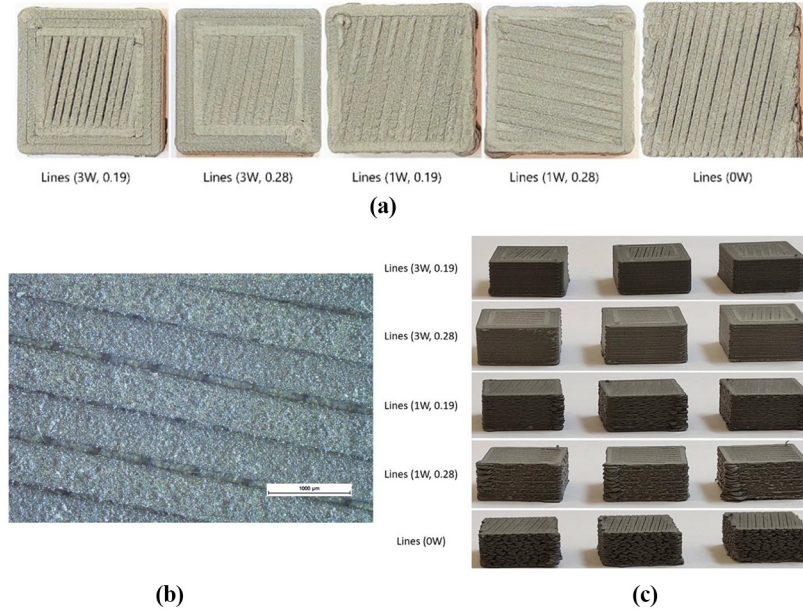
sample was also visually inspected to evaluate the lateral surface quality.

The *Concentric* infill specimens [Figure 7(a)] resulted in prints with relatively high porosity (i.e., 6.89%–8.35%, Table 3). Gaps were found between the printing lines [Figure 7(b)]. These defects are the most detrimental because they are repeated in each layer, compromising the structural stability of the component. Moreover, pores are evident at the beginning of the printing lines [Figure 7(a)]. External surfaces generally show good quality [Figure 7(c)].

Except for the *Lines* (0W), where the lack of the wall is detrimental [Figure 8(a)], the porosity values of the *Lines* infill samples are lower than those of the concentric ones (Table 3). The absence of walls causes the infill lines to detach [Figure 8(b)] and the specimen to sag, resulting in a bad printing quality inside the sample and on its lateral surfaces [Figure 8(c)]. With the same number of walls, the increase in the overlap reduces the porosity, but the quality of the external surface worsens. This effect is less pronounced when the number of walls is increased. However, this situation leads to a slight worsening of the porosity (i.e., from 0.20% to 0.83%, Table 3) because of gaps among the walls. Finally, compared to the concentric samples, in this case, the pores take the shapes of rectilinear channels [Figure 8(b)] rather than big concentric voids [Figure 7(b)] because the deposition orientation is inverted upon each layer completion.

The *Zig-zag* specimens [Figure 9(a)] have defects like those of the *Lines* samples. In addition, they show small voids near the walls [Figure 9(b)], which depend on the deposition path (see Figure 2). The increase of the overlap is beneficial to reduce the

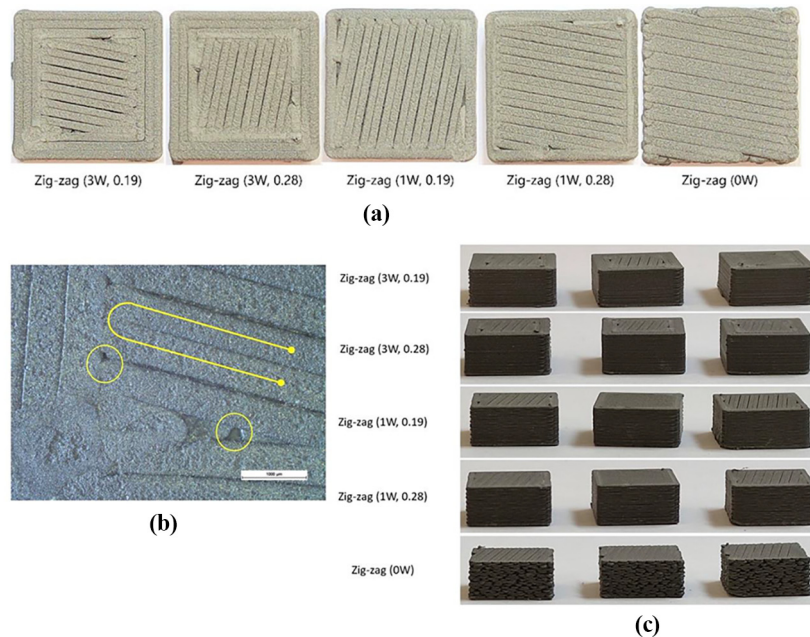
**Figure 8** Lines infill



**Notes:** (a) Picture of one specimen for each toolpath parameters combination; (b) optical microscope image of the most recurrent void channels; (c) all the printed specimens with a focus on their external surfaces

**Source:** Figure by authors

Figure 9 Zig-zag infill



**Notes:** (a) Picture of one specimen for each toolpath parameters combination; (b) a detail of the most recurrent defects: interconnected void channels and small voids near the walls; (c) all the printed specimens with a focus on their external surfaces

**Source:** Figure by authors

porosity, while there is a worsening for the print with no walls. Still, the worsening is less pronounced than in the *Lines* samples because the deposition lines are continuous in *Zig-zag* specimens. Indeed, the trend is similar to the sample with one wall and a reduced infill overlap [see (0W) and (1W,0.19) in Figure 9(a)]: the connection at the end of the line acted as a constraint, leading to a shape of the sample more similar to the theoretical one. As for *Lines* samples, the increase of the overlap negatively affects the external surface quality, but this effect is less pronounced than in the *Lines* samples due to the particular deposition path that links the extruded lines [Figure 9(c)].

In summary, over-extrusion is usually beneficial to reduce the internal porosity (i.e., the increase of the overlap), even if it could worsen the quality of the external surface and thus could demand further finishing processes after the sintering. Finally, the *Lines* infill demonstrated to be the most promising.

The results of the infill density investigation (second step, Figure 1) are reported in Table 4. The *Lines* (0W) was chosen for this investigation. This profile led to the lowest density value in the previous analysis (90.32%, Table 3). The sample was obtained with the C profile, i.e., with a 105% infill (Table 2). Hence, we wanted to investigate whether an increase in the infill density (120%, 135% and 150%) could influence the porosity. An almost perfect coverage was achieved in all cases, with density values higher than 99%. An increase in the infill from 105% to 120% raised the density from 90.32% to 99.74%. Over-extrusion occurred. It started from an infill equal to 135% and became more severe at 150% [Figure 10(a)], slightly worsening the porosity value. Moreover, this caused a build-up of material around the nozzle that hindered its movement and

**Table 4** Density (mean  $\pm$  standard deviation) and weight (mean  $\pm$  standard deviation) of the samples printed with 120%, 135%, and 150% infill

| Specimen        | Density ( $\mu \pm \sigma$ ) [%] | Weight ( $\mu \pm \sigma$ ) [g] |
|-----------------|----------------------------------|---------------------------------|
| 105%_Lines (0W) | 90.32 $\pm$ 0.20                 | 2.58 $\pm$ 0.02                 |
| 120%_Lines (0W) | 99.74 $\pm$ 0.23                 | 2.91 $\pm$ 0.02                 |
| 135%_Lines (0W) | 99.57 $\pm$ 0.18                 | 3.12 $\pm$ 0.13                 |
| 150%_Lines (0W) | 99.35 $\pm$ 0.11                 | 3.27 $\pm$ 0.00                 |

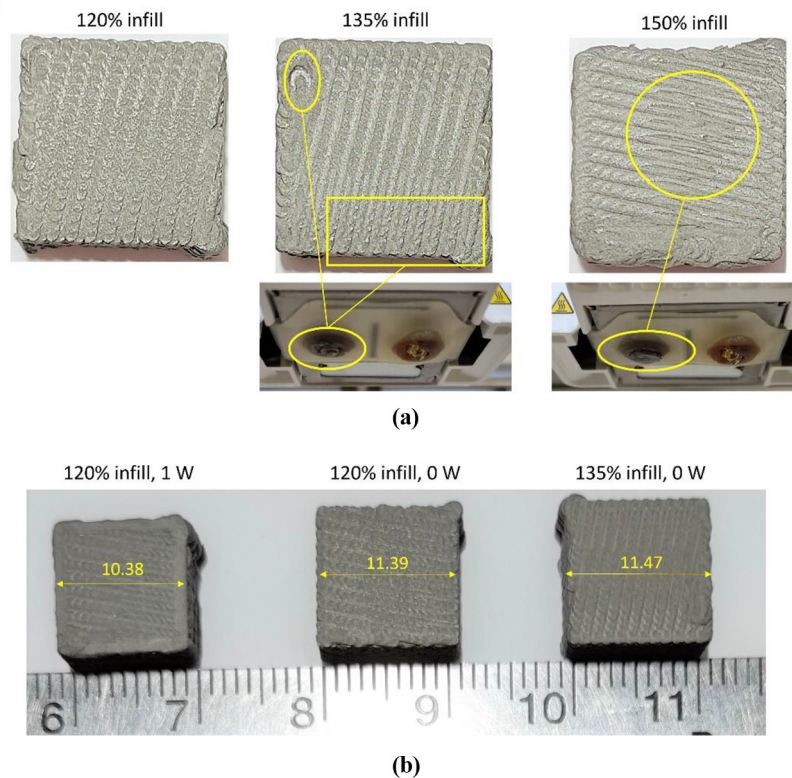
**Source:** Table by authors

determined clogging. Therefore, the best infill density value is 120%. It granted total layer coverage during printing and no noticeable over-extrusion.

The second drawback of increasing the infill density over 105% is the compromised dimensional accuracy. More material is extruded compared to the theoretical value needed to fill the nominal volume at 100% density, which generates heavier samples. Indeed, increasing the infill density in *Cura* reduces the infill line distance, which becomes smaller than the line width. Samples are also wider on the *xy* plane [Figure 10(b)] and slightly shorter than the nominal dimensions. Moreover, the external lateral surfaces are irregular, especially if zero-wall samples are printed, as in this analysis.

A further analysis (third step, Figure 1) was eventually devoted to investigating if, by changing the infill type and adding a wall structure, the dimensional accuracy could be preserved and a low porosity achieved. Results are reported in Table 5. The measurements of the dimensions indicate that all

**Figure 10** The influence of the infill density



**Notes:** (a) Over-extrusion signs on the printed samples at different infill densities and related material stuck on the nozzle (for the 120% and 135% infill); (b) combined influence of the infill density and wall count on the final dimensions of the printed parts (the theoretical dimension is 10 mm)

**Source:** Figure by authors

**Table 5** Average experimental values of the four types of specimens printed to investigate the dimensional accuracy of high-infill density green parts

| Specimen                | Weight ( $\mu \pm \sigma$ ) [g] | Length ( $\mu \pm \sigma$ ) [mm] | Width ( $\mu \pm \sigma$ ) [mm] | Height ( $\mu \pm \sigma$ ) [mm] |
|-------------------------|---------------------------------|----------------------------------|---------------------------------|----------------------------------|
| 3D model (theoretical)  | 2.35 (100%)                     | 10                               | 10                              | 5                                |
|                         | 2.82 (120%)                     |                                  |                                 |                                  |
| 120%_Lines (0W)         | 2.91 $\pm$ 0.02                 | 11.09 $\pm$ 0.03                 | 11.14 $\pm$ 0.04                | 4.93 $\pm$ 0.01                  |
| 120%_Lines, (1W, 0.19)  | 2.66 $\pm$ 0.00                 | 10.34 $\pm$ 0.01                 | 10.35 $\pm$ 0.03                | 4.96 $\pm$ 0.01                  |
| 120%_Zig-zag (0W)       | 2.74 $\pm$ 0.03                 | 10.57 $\pm$ 0.08                 | 10.6 $\pm$ 0.12                 | 4.95 $\pm$ 0.02                  |
| 120%_Zig-zag (1W, 0.19) | 2.67 $\pm$ 0.02                 | 10.42 $\pm$ 0.02                 | 10.47 $\pm$ 0.03                | 4.97 $\pm$ 0.03                  |

**Notes:** The theoretical weight was calculated considering a green density equal to 4.7 g/cm<sup>3</sup>, reported in the Debinding Simulation Guidelines provided by BASF (2022)

**Source:** Table by authors

the specimens suffered from sagging in different ways: the base sizes were bigger, while the heights were smaller, compared to the nominal values. This effect was more pronounced in the cases of specimens without the wall. Comparing the two prints without the wall, it is possible to see that the *Zig-zag* one had a better shape accuracy, probably due to the rounds that connect consecutive lines [Figure 10(b)].

In summary, all the samples present a central zone, which could be assumed to be nearly dense, and an irregular external shell. These results show that obtaining near-dense parts with a

proper choice of parameters is possible, even if the drawback is an inaccurate replica of their theoretical shape. Figure 10(b) also shows another interesting aspect, i.e., increasing the infill density without using walls worsens the discrepancy between the theoretical and the real dimensions of the printed part.

### 3.2 Characterisation of the sintered parts

#### 3.2.1 Density and porosity investigation

The density of the sintered parts measured by Archimedes' method and their apparent porosity are reported in Table 6.

**Table 6** Results of the metal specimens' density and porosity investigation

| Specimen                 | Density ( $\mu \pm \sigma$ ) [g/cm <sup>3</sup> ] | Average apparent porosity [%] |
|--------------------------|---|-------------------------------|
| 105%_Concentric (10)     | 7.05 ± 0.23                                       | 11.89                         |
| 105%_Concentric (10;45°) | 7.01 ± 0.15                                       | 12.41                         |
| 105%_Concentric (12)     | 7.00 ± 0.33                                       | 12.49                         |
| 105%_Lines (3W, 0.19)    | 7.21 ± 0.21                                       | 9.83                          |
| 105%_Lines (3W, 0.28)    | 7.22 ± 0.28                                       | 9.79                          |
| 105%_Lines (1W, 0.19)    | 7.24 ± 0.24                                       | 9.55                          |
| 105%_Lines (1W, 0.28)    | 7.19 ± 0.19                                       | 10.12                         |
| 105%_Lines (0W)          | 7.05 ± 0.30                                       | 11.82                         |
| 105%_Zig-zag (3W, 0.19)  | 7.12 ± 0.27                                       | 11.06                         |
| 105%_Zig-zag (3W, 0.28)  | 7.28 ± 0.29                                       | 8.99                          |
| 105%_Zig-zag (1W, 0.19)  | 7.17 ± 0.21                                       | 10.38                         |
| 105%_Zig-zag (1W, 0.28)  | 7.28 ± 0.25                                       | 9.03                          |
| 105%_Zig-zag (0W)        | 7.16 ± 0.24                                       | 10.46                         |
| 120%_Lines (0W)          | 7.37 ± 0.11                                       | 7.92                          |
| 120%_Lines (1W, 0.19)    | 7.38 ± 0.13                                       | 7.79                          |
| 120%_Zig-zag (0W)        | 7.36 ± 0.12                                       | 7.98                          |
| 120%_Zig-zag (1W, 0.19)  | 7.37 ± 0.09                                       | 7.90                          |

**Notes:** For each sample, the density (mean ± standard deviation) measured with the hydrostatic balance and the average apparent porosity, obtained by comparing the density value with the theoretical one, are reported

**Source:** Table by authors

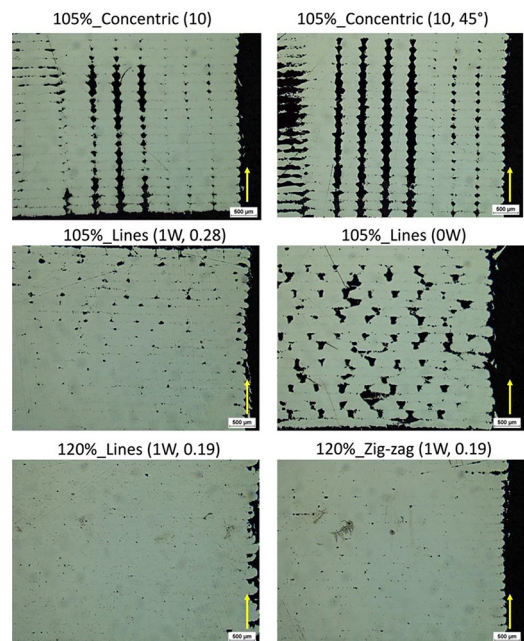
The results of the samples printed with an infill density equal to 105% agree with those already discussed. The concentric infill determines the bigger apparent porosity among the three different types due to the poor coverage of the material in each layer. The *Concentric* and *Zig-zag* infill results reach similar values, with a maximum density of 7.28 g/cm<sup>3</sup> for the two *Zig-zag* specimens with the highest overlap. As expected, the specimens with an infill density of 120% showed a higher density than the 105% infill density specimens. The differences between the porosity evaluated in the green and in the metal specimen, as well as the low measured density values, are due to limitations of the used method. Due to the printing process, air is present in close pores, and it cannot escape during the density measurement, contributing to the buoyancy of the sample.

The porosity was also qualitatively evaluated by image analysis of LOM micrographs. Representative sections of samples parallel to the building direction are provided in [Figure 11](#). The picture comparison shows a separation layer made by pores located in planes between deposited layers in the 105% specimen. In contrast, a homogeneous structure is obtained in the 120% infill specimen. Only small pores are visible in the latter, without any preferential position.

### 3.2.2 Tensile testing

The stress–strain curves of 3D-printed and MIM specimens are reported in [Figure 12\(a\)](#). One of the *Lines* specimens failed earlier than expected during testing. No noticeable differences in the curves were found between *Lines* and *Zig-zag* specimens. Yield strength ( $R_{p0.2}$ ), UTS, and elongation at fracture (A) of the MFFF and MIM samples are reported in [Table 7](#).

The  $R_{p0.2}$  of the 3D-printed samples were higher than those found by other studies on the same material; moreover, they are also higher than those obtained by testing MIM samples, indicating the potential of MFFF to compete with established manufacturing technologies. However, for both infill types, the

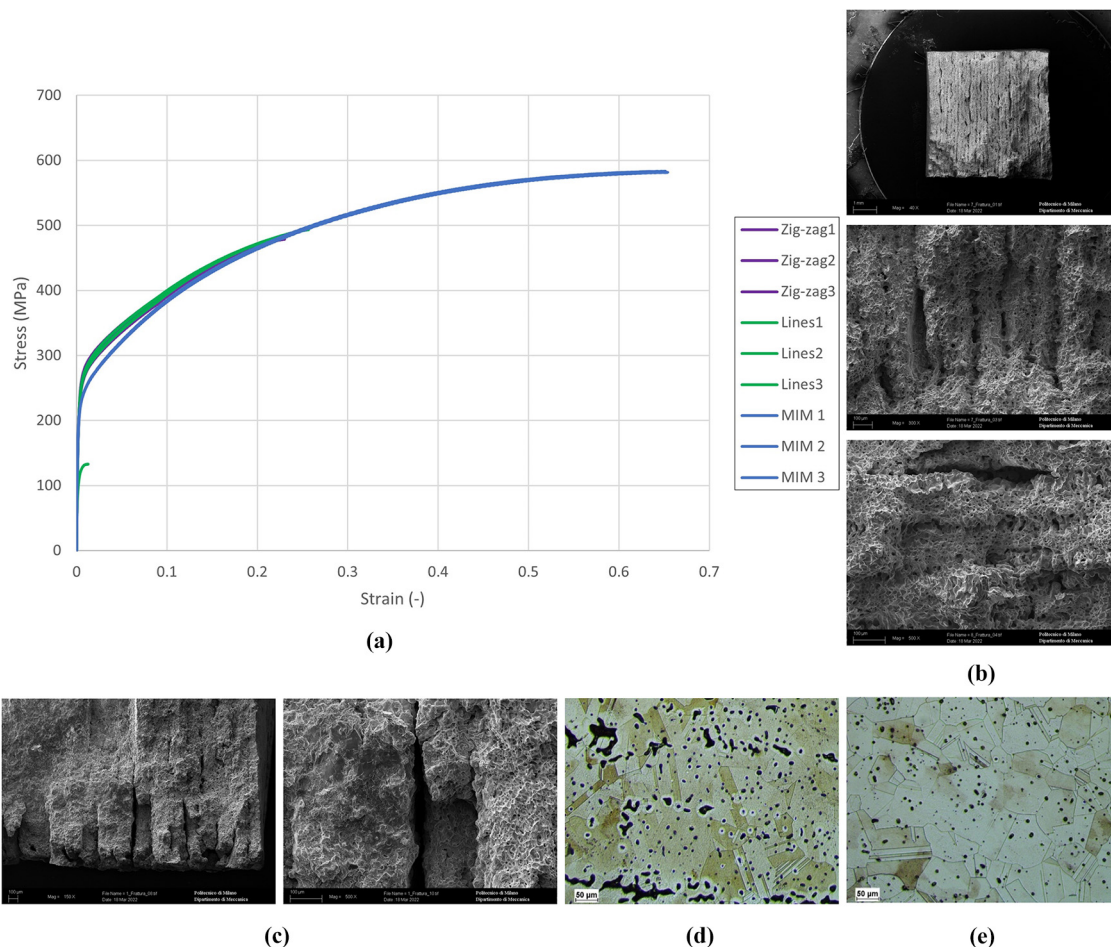
**Figure 11** Examples of LOM pictures of the section of the metal specimens used for the porosity evaluations

**Note:** The arrow indicates the print direction

**Source:** Figure by authors

values were lower than those reported in the BASF specification. The A (i.e., elongation at fracture in [Table 7](#)) of MFFF samples was significantly lower than that of MIM samples and reported by BASF. Due to the low elongation at break, the UTS was also low. The SEM analysis of the fracture surfaces explained the lower mechanical properties of the

**Figure 12** Tensile properties and microstructural analysis



**Notes:** (a) Stress-strain curves of the 6 dogbonespecimens printed using Zig-Zag and Lines infill types and of the 3 MIM specimens; (b) SEMimages of the fracture surface, with evidence of layering and dimples indicating a ductile fracture;(c) SEM images of the fracture surface of the “Lines 2” specimen (early failure), with signs of delamination and crack formation; (d) microstructure of the 3D-printed sample; (e) microstructure of the MIM sample

**Source:** Figure by authors

printed samples: the layered structure is visible [Figure 12(b)], with pores that inevitably affect the mechanical performance. Table 7 also reports the results recently obtained by Caminero *et al.* (2022), Obadimu *et al.* (2022), and Pellegrini *et al.* (2022). These studies confirm the similar mechanical properties of flat and on-edge samples. Comparing our results with those reported by the authors for their flat specimens, it is possible to observe that higher yield strengths are achieved in this study, probably due to the slightly higher infill density (105 vs 100%) positively affecting material density. The UTS of the *Lines* specimens is similar to that obtained by Caminero *et al.* (2022) and higher than that achieved by Pellegrini *et al.* (2022) and Obadimu *et al.* (2022).

Moreover, closer inspections allow for distinguishing porosities created during the sintering from cavities created during the deposition process. The surfaces showed characteristics typical of ductile fractures, with the presence of dimples [Figure 12(b)]. As expected, no dimples were visible

on the cavities between layers. Therefore, those regions have negatively influenced the mechanical properties of the material. From the analysis of the fracture surface of the *Lines 2* sample [Figure 12(c)], which failed earlier than expected, a crack near the surface due to delamination during printing was found. The oxide was identified on the side of the crack, likely created during sintering and annealing.

The microstructure of the 3D-printed and MIM parts was inspected by LOM [Figure 12(d)–(e)]. In both cases, the annealed material was characterised by equiaxed austenitic grains with annealing twins. The morphology of the grains was independent of the printing direction. Round micropores with a diameter lower than 10  $\mu\text{m}$  were found inside the material. Such pores are typical of sintered materials and cannot be avoided. Additionally, bigger pores were in the 3D-printed specimens, arranged on parallel planes between adjacent deposition layers. No coarse inclusions, carbides or oxides were found. Even if not analysed in the present study, a possible

solution to achieve pore closure and enhanced mechanical properties is by performing hot isostatic pressing (HIP) during the sintering phase. In Wang *et al.* (2021), this technique was applied to 316L parts obtained by MFFF. By comparing micro-CT analysis of the green and the corresponding HIP-sintered samples, the authors demonstrated that the treatment allows the closing of elongated porosities due to the printing process. Moreover, HIP-sintered samples have higher and more isotropic mechanical properties than those only sintered.

### 3.3 Investigation of manufacturability limits: DfAM rules and cellular structures

The first printed prototypes are shown in Figure 13. The bridge structures [Figure 13(a)] were printed on a thin base, which warped during printing. In all bridges, the first layers were not correctly printed, and sagging of the structure was evident. All the bridges collapsed during the debinding phase, apart from the 5 mm one, which could be considered the limit value. However, in the 5 mm bridge, we can also notice a crack on the top surface that became evident after the debinding. The four horizontal holes were successfully printed, debinded, and sintered [Figure 13(b)]. The overhang angles were also printed and sintered without defects [Figure 13(c)]. As regards the unsupported edges, sagging was observed in all edges equal or wider to two times the extrusion width [i.e., starting from 1.2 mm, Figure 13(d)]. Moreover, during sintering, a crack occurred on the upper face of the sample. However, this crack is not related to unsupported surfaces but to internal stresses.

The results of the analysed features can be summarised as follows:

- The maximum overhang for the bridge feature is 5 mm, though a small crack formed on the top after sintering.
- Horizontal holes up to 6 mm in diameter can be printed and subjected to D&S.
- Unsupported edges are printable up to 2.4 mm, but with protrusion bigger than 1.2 mm, the first few layers suffer sagging. This risk could be reduced by adding a fillet between the bottom surface of the overhang and the vertical wall.
- Sloped surfaces at 35° can be printed and D&S successfully.

Figure 14 shows the lattices that were printed, and some of them were also debinded and sintered. The body-centred cubic (BCC) unit cell [Figure 14(a)] broke during the detachment from the printing bed, probably due to the too-low thickness of its beams (1 mm). The same structure was 3D-printed using a PVA brim. The cell was successfully detached from the print bed. Figures 14(b) and 14(c) show two successfully printed simple cubic (SC) lattice examples: one 2×2×3 and one 3×3×4 array. However, the 3×3×4 array broke during the D&S step due to the small dimensions. Figure 14(d) shows a 2×3×5 matrix-based Schwarz-Primitive (wall thickness of 0.7 mm), with signs of delamination between layers. The bottom part broke during the D&S heat treatment. Figure 14(e) shows a 3×3×5 network-based IWP. It was successfully printed, debinded and sintered, but signs of delamination were visible. In Figure 14(f), a broken matrix-based Gyroid cell is shown. It was printed using the PVA supports; unfortunately, some filaments of PVA were printed between UF316L layers, drastically reducing

the cohesion between them and leading to failure during part removal. Hence, a lateral wall was added to print Gyroid structures and to create a network-based Gyroid, obtaining good results both at high (50%) and low (20%) volume fractions [Figure 14 (g)–(i)] and for different cell sizes. To test the versatility of the process, a 2×2×2 network-based Gyroid and a 1×1×2 network-based Gyroid array with lateral walls and linear volume fraction gradient were successfully printed, debinded and sintered [Figure 14 (j)–(k)]. However, as shown in Figure 14(j), the surface is no longer continuous when the structure thickness decreases substantially.

These examples demonstrate that thanks to the proper tailoring of the printing parameters, it is possible to print even complex metal structures using the MFFF technology. However, there are limitations given not only by the standard FFF rules, but also because the component undergoes a D&S process. Clarifying the influence of each step would be relevant, and it can be considered a possible future work together with the mechanical characterisation of the manufactured lattice samples. Their mechanical properties could be compared with those printed via LPBF. Finally, those lattices subjected to D&S have shown the expected shrinkage.

## 4. Conclusions

This study analyses the properties of green and sintered parts obtained by MFFF and a commercial 316L filament. It proves the possibility of using FFF to produce metal parts. The following insights have been derived.

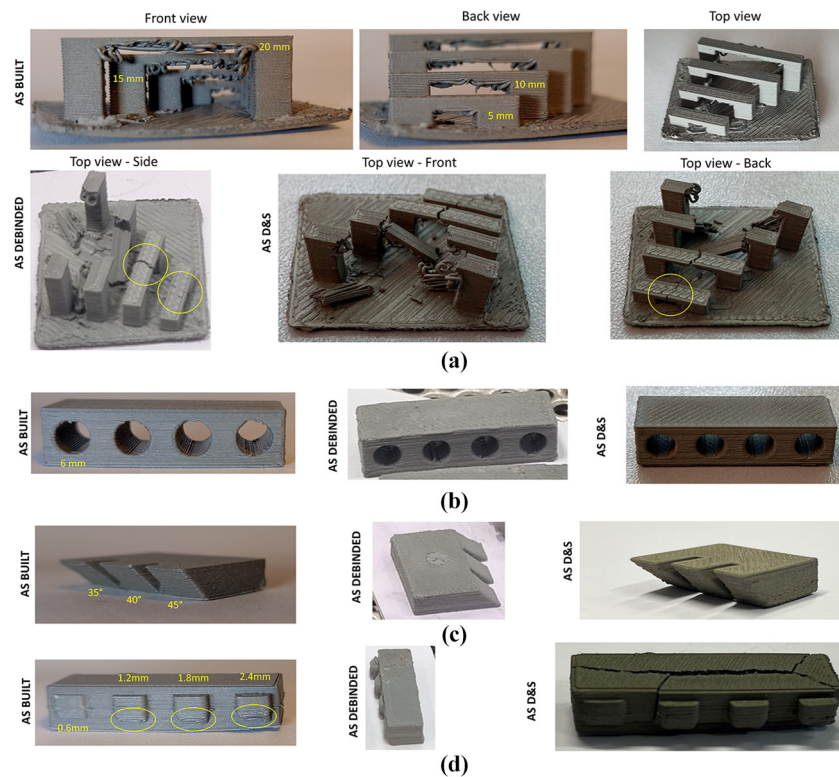
- When printing the UF316L filament, a nozzle temperature of 240°C and bed temperature of 100° are required to produce successful prints; hairspray is essential to avoid detachment from the printing bed.
- The choice of the appropriate toolpath parameters drastically changes the relative density of the green parts, with the type of the infill playing the most relevant role; *Lines* and *Zig-zag* infills allow better material distribution compared to *Concentric* infill.
- Green parts with a relative density above 99% can be printed by increasing the infill density. A value of 120% is enough to close voids created during material deposition.
- The density of the green parts printed with 120% infill density is 7.37 g/cm<sup>3</sup>, lower than that declared by BASF for the green. Limitations of the used method could have affected this measurement.
- The relative density of the sintered parts conforms to the values of the relative density of the green parts.
- Voids accumulate in parallel planes at the interfaces between layers.
- The microstructure of the steel is homogenous, with equiaxed austenite grains and the presence of annealing twins. No coarse second phases are present in the sintered specimens.
- The mechanical properties of the 3D-printed annealed material are  $R_{p0.2} = 233.0$  MPa, UTS = 486.5 MPa and  $A = 25.0\%$ . Such values are comparable to those achieved in previous studies.
- Design guidelines that consider the printing and the D&S phases have been derived. The following geometric features can be successfully printed, debinded and sintered: maximum bridge overhang of 5 mm, horizontal

**Table 7** Yield strength( $R_{p0,2}$ ), ultimate tensile strength (UTS), and elongation at fracture (A) from the 3D-printed specimens, MIM specimens, BASF data sheet, studies from [Caminero et al. \(2022\)](#), [Obadimu et al. \(2022\)](#), and [Pellegrini et al. \(2022\)](#)

| Specimen                                 | Infill density [%] | Infill type | Printing orientation | $R_{p0,2}$ [MPa] | UTS [MPa]    | A [%]      |
|--|--------------------|-------------|----------------------|------------------|--------------|------------|
| BASF                                     | 105                | Lines       | Flat x–y             | 251              | 561          | 53         |
|  |                    |             | Upright z            | 234              | 521          | 36         |
| This study                               | 105                | Zig-zag     | Flat x               | 233.3 ± 7.1      | 474.3 ± 7.2  | 23.5 ± 1.7 |
|  |                    | Lines       |                      | 233.0 ± 0.1      | 486.5 ± 10.6 | 25.0 ± 2.5 |
| <a href="#">Caminero et al. (2022)</a>   | 100                | Concentric  | Flat x               | 184.6 ± 4.9      | 495.1 ± 5.3  | 35.4 ± 1.2 |
|  |                    |             | On-edge x            | 188.1 ± 5.2      | 497.3 ± 4.3  | 37.6 ± 0.8 |
| <a href="#">Obadimu et al. (2022)</a>    | 100                | Lines       | Flat x               | 146.4            | 421.8        | 35.4       |
| <a href="#">Pellegrini et al. (2022)</a> | 100                | Lines       | Flat x               | 125.7            | 405.2        | 45         |
|  |                    |             | On-edge x            | 132.7            | 439.3        | 43         |
|  |                    |             | Upright z            | 122.7            | 399.6        | 35         |
| MIM                                      |                    |             |                      | 210.7 ± 3.5      | 583.0 ± 1.0  | 73.6 ± 0.9 |

**Note:** Only the maximum average value obtained for each printing orientation is reported for the study from [Pellegrini et al., \(2022\)](#)  
Source: Table by authors

**Figure 13** 3D-printed (as built), debinded and sintered prototypes of the four types of features analysed ([Figure 4](#)): (a) bridges; (b) horizontal holes; (c) overhang angles and (d) unsupported edges



**Source:** Figure by authors

holes up to 6 mm in diameter, unsupported edges up to two times the extrusion width and sloped surfaces at an inclination up to 35°.

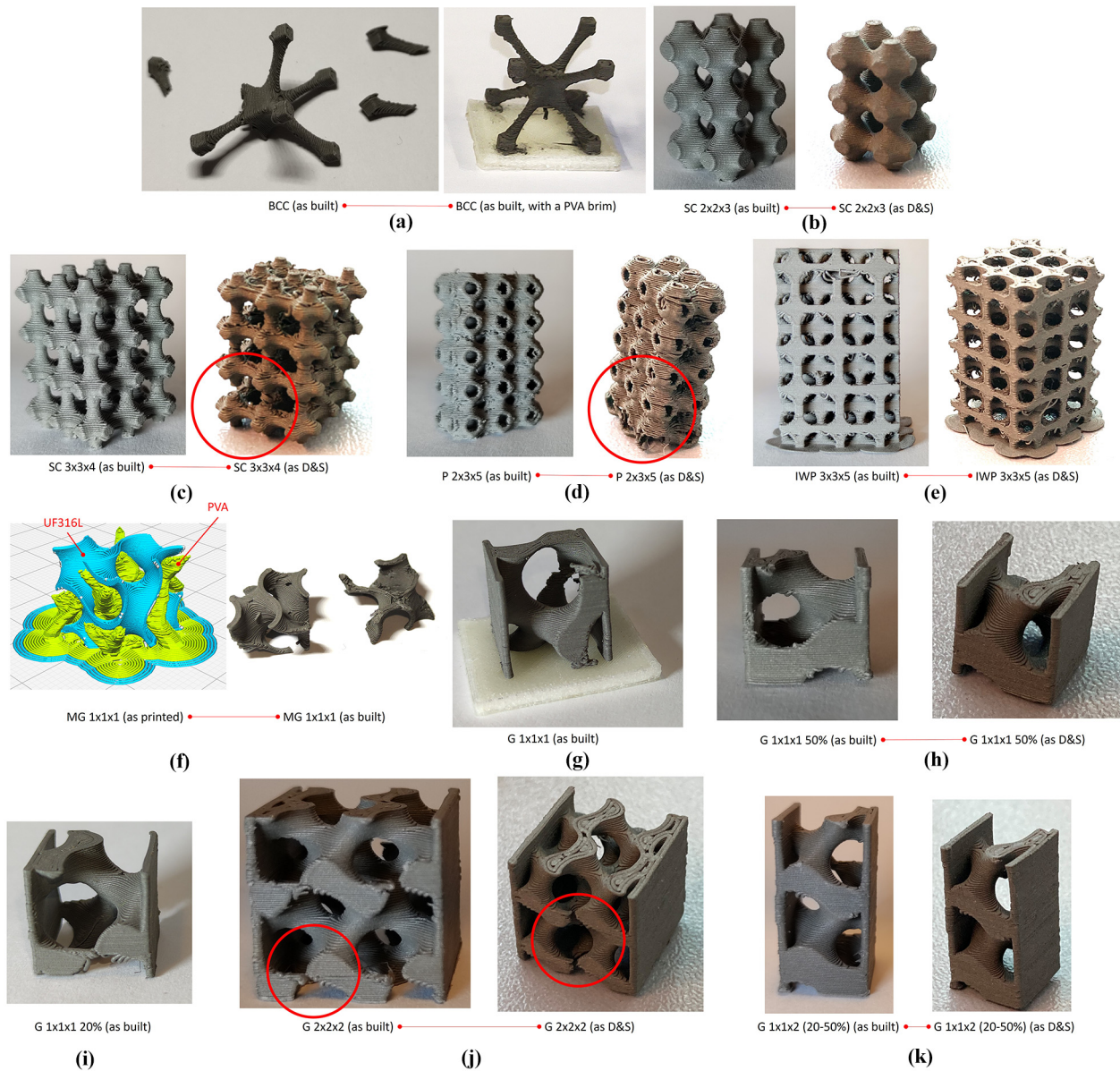
- Strut-and-node and TPMS cellular structures can be successfully manufactured if printing and D&S constraints are considered.

To conclude, the continuous efforts to improve the printability of metal-based filaments, combined with the growing scientific

literature on this topic, are strengthening the high potential of FFF technology in metal AM. Compared to the existing studies, this work extensively investigates multiple process and design aspects. It also demonstrates the feasibility of fabricating both metallic bulk components and cellular structures. Printing strut-and-node and TPMS-based structures is a significant step forward compared to already manufactured lattices using the 316L material, which were “wall-based” (plate-based and honeycomb structures). Therefore, it projects MFFF as a



Figure 14 Examples of 3D-printed cellular structures



**Notes:** Some have also been debinded and sintered (the corresponding 3D model of each structure is provided in Figure 5). (a) Broken BCC cell and the same printed using a PVA support; (b-c) SC lattice structures (2x2x3 and 3x3x4) as built and as D&S; (d) Matrix-based Schwarz-Primitive array (2x3x5) as built and as D&S; (e) Network-based IWP 3x3x5 structure, as built and as D&S; (f) Matrix-based Gyroid as printed with PVA and as-built after the removal from the print bed; (g) Network-based Gyroid single cell with lateral walls and PVA brim (as built); (h) Network-based Gyroid with 50% volume fraction and lateral walls as built and as D&S; (i) Network-based Gyroid with 20% volume fraction and lateral walls as built; (j) Network-based Gyroid 2x2x2 structure with lateral walls as built and as D&S; (k) Network-based Gyroid 1x1x2 structure with lateral walls and volume fraction gradient as built and D&S

**Source:** Figure by authors

potentially cost-effective and valid alternative to more expensive metal AM technologies for various applications requiring lightweighting, mechanical performance, and design customisation. Furthermore, the combined use of biocompatible materials, such as 316L stainless steel or titanium alloys, also allows its adoption for biomedical applications, such as the fabrication of metallic implants, as already documented in the literature (Gloeckle et al.,

2020; Shaikh et al., 2021b). However, further research focused on deepening the relationship between process parameters and mechanical properties, combined with studies about optimised post-processing treatments, is fundamental to unlocking the full potential of MFFF and making it compete with more established metal AM technologies to produce end-use products.

## References

- Ait-Mansour, I., Kretschmar, N., Chekurov, S., Salmi, M. and Rech, J. (2020), “Design-dependent shrinkage compensation modeling and mechanical property targeting of metal FFF”, *Progress in Additive Manufacturing*, Vol. 5 No. 1, pp. 51-57.
- ASTM (2020), “ASTM E8/E8M standard test methods for tension testing of metallic materials”, doi: [10.1520/E0008](https://doi.org/10.1520/E0008).
- Bankapalli, N.K., Gupta, V., Saxena, P., Bajpai, A., Lahoda, C. and Polte, J. (2023), “Filament fabrication and subsequent additive manufacturing, debinding, and sintering for extrusion-based metal additive manufacturing and their applications: a review”, *Composites Part B: Engineering*, Elsevier Ltd, Vol. 264, p. 110915.
- BASF (2021), “Ultrafuse® metal filaments technical data sheet for 3D printing metal parts”, available at: [https://move.forward-am.com/hubfs/AESDocumentation/MetalFilaments/316L/TDS/Ultrafuse\\_316L\\_TDS\\_EN\\_v1.1.pdf](https://move.forward-am.com/hubfs/AESDocumentation/MetalFilaments/316L/TDS/Ultrafuse_316L_TDS_EN_v1.1.pdf) (accessed 12 September 2023).
- BASF (2022), “Ultrafuse 316L 3D printer metal filament | BASF forward AM”, available at: <https://forward-am.com/material-portfolio/ultrafuse-filaments-for-fused-filaments-fabrication-fff/metal-filaments/ultrafuse-316l/> (accessed 12 September 2023).
- Bocchi, S., D’Urso, G., Giardini, C., Carminati, M., Borriello, C., Tammaro, L. and Galvagno, S. (2024), “Reuse of green parts for metal material extrusion: a recycling approach for improved sustainability”, *Journal of Cleaner Production*, Vol. 434, p. 140165.
- Boschetto, A., Bottini, L., Miani, F. and Veniali, F. (2022), “Roughness investigation of steel 316L parts fabricated by metal fused filament fabrication”, *Journal of Manufacturing Processes*, Vol. 81, pp. 261-280.
- Camínero, M.Á., Romero Gutiérrez, A., Chacón, J.M., García-Plaza, E. and Núñez, P.J. (2022), “Effects of fused filament fabrication parameters on the manufacturing of 316L stainless-steel components: geometric and mechanical properties”, *Rapid Prototyping Journal*, Vol. 28 No. 10, pp. 2004-2026.
- Camínero, M.Á., Romero, A., Chacón, J.M., Núñez, P.J., García-Plaza, E. and Rodríguez, G.P. (2021), “Additive manufacturing of 316L stainless-steel structures using fused filament fabrication technology: mechanical and geometric properties”, *Rapid Prototyping Journal*, Vol. 27 No. 3, pp. 583-591.
- Carminati, M., Quarto, M., D’Urso, G., Giardini, C. and Maccarini, G. (2022), “Mechanical characterization of AISI 316L samples printed using material extrusion”, *Applied Sciences*, Vol. 12 No. 3, doi: [10.3390/app12031433](https://doi.org/10.3390/app12031433).
- Cuan-Urquiza, E., Barocio, E., Tejada-Ortigoza, V., Pipes, R.B., Rodríguez, C.A. and Roman-Flores, A. (2019), “Characterization of the mechanical properties of FFF structures and materials: a review on the experimental, computational and theoretical approaches”, *Materials*, Vol. 12 No. 6, doi: [10.3390/ma12060895](https://doi.org/10.3390/ma12060895).
- Damon, J., Dietrich, S., Gorantla, S., Popp, U., Okolo, B. and Schulze, V. (2019), “Process porosity and mechanical performance of fused filament fabricated 316L stainless steel”, *Rapid Prototyping Journal*, Vol. 25 No. 7, pp. 1319-1327.
- Gloeckle, C., Konkol, T., Jacobs, O., Limberg, W., Ebel, T. and Handge, U.A. (2020), “Processing of highly filled polymer-metal feedstocks for fused filament fabrication and the production of metallic implants”, *Materials*, Vol. 13 No. 19, pp. 1-16.
- Gong, H., Snelling, D., Kardel, K. and Carrano, A. (2019), “Comparison of stainless steel 316L parts made by FDM- and SLM-based additive manufacturing processes”, *JOM*, Vol. 71 No. 3, pp. 880-885.
- Gong, H., Crater, C., Ordóñez, A., Ward, C., Waller, M. and Ginn, C. (2018), “Material properties and shrinkage of 3D printing parts using ultrafuse stainless steel 316LX filament”, *MATEC Web of Conferences*, Vol. 249, doi: [10.1051/mateconf/201824901001](https://doi.org/10.1051/mateconf/201824901001).
- Gonzalez-Gutierrez, J., Cano, S., Schuschnigg, S., Kukla, C., Sapkota, J. and Holzer, C. (2018), “Additive manufacturing of metallic and ceramic components by the material extrusion of highly-filled polymers: a review and future perspectives”, *Materials*, Vol. 11 No. 5, doi: [10.3390/ma11050840](https://doi.org/10.3390/ma11050840).
- Guerra Silva, R., Torres, M.J., Zahr Vinuela, J. and Zamora, A.G. (2021), “Lattice structures using fused filament fabrication”, *Polymers*, Vol. 13 No. 4.
- HUBS (2022), “Design rules for 3D printing poster”, available at: [www.hubs.com/get/3d-printing-design-rules/](http://www.hubs.com/get/3d-printing-design-rules/) (accessed 12 September 2023).
- Hydra Research 3D (2022), “Design rules for FFF 3D printing”, available at: [www.hydraresearch3d.com/design-rules](http://www.hydraresearch3d.com/design-rules) (accessed: 12 September 2023).
- ISO (2009), “ISO 2740 sintered metal materials, excluding hardmetals – tensile test pieces”.
- Jiang, D. and Ning, F. (2021), “Additive manufacturing of 316L stainless steel by a printing-debinding-sintering method: effects of microstructure on fatigue property”, *Journal of Manufacturing Science and Engineering*, Vol. 143 No. 9, pp. 1-10.
- Jiang, D. and Ning, F. (2022a), “Anisotropic deformation of 316L stainless steel overhang structures built by material extrusion based additive manufacturing”, *Additive Manufacturing*, Vol. 50, p. 102545.
- Jiang, D. and Ning, F. (2022b), “Physical-mechanical behaviors of stainless steel plate-lattice built by material extrusion additive manufacturing”, *Journal of Materials Processing Technology*, Vol. 309, p. 117739.
- Jimbo, K. and Tateno, T. (2019), “Shape contraction in sintering of 3d objects fabricated via metal material extrusion in additive manufacturing”, *International Journal of Automation Technology*, Vol. 13 No. 3, pp. 354-360.
- Kasha, A., Obadimu, S.O. and Kourousis, K.I. (2022), “Flexural characteristics of material extrusion steel 316L: influence of manufacturing parameters”, *Additive Manufacturing Letters*, Vol. 3, p. 100087.
- Liu, B., Wang, Y., Lin, Z. and Zhang, T. (2020), “Creating metal parts by fused deposition modeling and sintering”, *Materials Letters*, Vol. 263, p. 127252.
- Maskery, I., Parry, L.A., Padrão, D., Hague, R.J.M. and Ashcroft, I.A. (2022), “FLatt pack: a research-focussed lattice design program”, *Additive Manufacturing*, Vol. 49, doi: [10.1016/j.addma.2021.102510](https://doi.org/10.1016/j.addma.2021.102510).

- Medellin-Castillo, H.I. and Zaragoza-Siqueiros, J. (2019), "Design and manufacturing strategies for fused deposition modelling in additive manufacturing: a review", *Chinese Journal of Mechanical Engineering*, Vol. 32 No. 1, pp. 1-16.
- Moritzer, E., Elsner, C.L. and Schumacher, C. (2021), "Investigation of metal-polymer composites manufactured by fused deposition modeling with regard to process parameters", *Polymer Composites*, Vol. 42 No. 11, pp. 6065-6079.
- Obadimu, S.O. and Kourousis, K.I. (2022a), "Shrinkage behaviour of material extrusion steel 316L: influence of primary 3D printing parameters", *Rapid Prototyping Journal*, Vol. 28 No. 11, pp. 92-101.
- Obadimu, S.O. and Kourousis, K.I. (2022b), "Load-rate effects on the in-plane compressive behaviour of additively manufactured steel 316L honeycomb structures", *Engineering Structures*, Vol. 273, p. 115063.
- Obadimu, S.O., Kasha, A. and Kourousis, K.I. (2022), "Tensile performance and plastic anisotropy of material extrusion steel 316L: influence of primary manufacturing parameters", *Additive Manufacturing, Elsevier B.V.*, Vol. 60, p. 103297.
- Pellegrini, A., Palmieri, M.E. and Guerra, M.G. (2022), "Evaluation of anisotropic mechanical behaviour of 316L parts realized by metal fused filament fabrication using digital image correlation", *The International Journal of Advanced Manufacturing Technology*, Vol. 120 Nos 11/12, pp. 7951-7965.
- Quarto, M., Carminati, M. and D'Urso, G. (2021), "Density and shrinkage evaluation of AISI 316L parts printed via FDM process", *Materials and Manufacturing Processes*, Vol. 36 No. 13, pp. 1535-1543.
- Rosnitschek, T., Tremmel, S., Seefeldt, A., Alber-Laukant, B., Neumeyer, T. and Altstädt, V. (2021), "Correlations of geometry and infill degree of extrusion additively manufactured 316l stainless steel components", *Materials*, Vol. 14 No. 18, doi: [10.3390/ma14185173](https://doi.org/10.3390/ma14185173).
- Shaikh, M.Q., Graziosi, S. and Atre, S.V. (2021a), "Supportless printing of lattice structures by metal fused filament fabrication (MF3) of Ti-6Al-4V: design and analysis", *Rapid Prototyping Journal*, Vol. 27 No. 7, pp. 1408-1422.
- Shaikh, M.Q., Nath, S.D., Akilan, A.A., Khanjar, S., Balla, V.K., Grant, G.T. and Atre, S.V. (2021b), "Investigation of patient-specific maxillofacial implant prototype development by metal fused filament fabrication (Mf3) of ti-6al-4v", *Dentistry Journal*, Vol. 9 No. 10, doi: [10.3390/dj9100109](https://doi.org/10.3390/dj9100109).
- Steuben, J., Van Bossuyt, D.L. and Turner, C. (2015), "Design for fused filament fabrication additive manufacturing", *International Design Engineering Technical Conferences and Computers and Information in Engineering Conference. American Society of Mechanical Engineers*, Vol. 4, [10.1115/DETC2015-46355](https://doi.org/10.1115/DETC2015-46355).
- Suwanpreecha, C. and Manonukul, A. (2022), "A review on material extrusion additive manufacturing of metal and how it compares with metal injection moulding", *Metals*, Vol. 12 No. 3, p. 429.
- Thompson, Y., Gonzalez-Gutierrez, J., Kukla, C. and Felfer, P. (2019), "Fused filament fabrication, debinding and sintering as a low cost additive manufacturing method of 316L stainless steel", *Additive Manufacturing, Elsevier*, Vol. 30, p. 100861.
- Tosto, C., Tirillò, J., Sarasini, F. and Cicala, G. (2021), "Hybrid metal/polymer filaments for fused filament fabrication (FFF) to print metal parts", *Applied Sciences (Switzerland)*, Vol. 11 No. 4, p. 1.
- Turner, B.N. and Gold, S.A. (2015), "A review of melt extrusion additive manufacturing processes: II. Materials, dimensional accuracy, and surface roughness", *Rapid Prototyping Journal*, Vol. 21 No. 3, pp. 250-261.
- Ultimaker (2022a), "Ultimaker S5", available at: <https://ultimaker.com/3d-printers/ultimaker-s5> (accessed 12 September 2023).
- Ultimaker (2022b), "Infill settings", available at: <https://support.ultimaker.com/s/article/1667411002588> (accessed 26 September 2023).
- Wagner, M.A., Hadian, A., Sebastian, T., Clemens, F., Schweizer, T., Rodriguez-Arbaizar, M., Carreño-Morelli, E. and Spolenak, R. (2022), "Fused filament fabrication of stainless steel structures - from binder development to sintered properties", *Additive Manufacturing*, Vol. 49, doi: [10.1016/j.addma.2021.102472](https://doi.org/10.1016/j.addma.2021.102472).
- Wang, Y., Zhang, L., Li, X. and Yan, Z. (2021), "On hot isostatic pressing sintering of fused filament fabricated 316L stainless steel - evaluation of microstructure, porosity, and tensile properties", *Materials Letters*, Vol. 296, p. 129854.

### Supplementary material

The supplementary material for this article can be found online.

### Corresponding author

Serena Graziosi can be contacted at: [serena.graziosi@polimi.it](mailto:serena.graziosi@polimi.it)